RSC Advances

PAPER

View Article Online
View Journal | View Issue

Check for updates

Cite this: RSC Adv., 2022, 12, 9883

Optoelectronic properties and interfacial interactions of two-dimensional Cs_2PbX_4–MSe_2 (M = Mo, W) heterostructures

Ying Jie Chen,[ab] Xue Li,[b] Bao Nan Jia,[b] Chao Dong,[b] Xiao Ning Guan,*[bd] Xin Zhao[a] and Li Hong Han*[abc]

Received 28th January 2022
Accepted 6th March 2022

DOI: 10.1039/d2ra00595f

rsc.li/rsc-advances

Constructing 2D inorganic perovskites and TMDs heterostructures is an effective method to design stable and high-performance perovskites optoelectronic applications. Here, we investigate the optoelectronic properties and interfacial interactions of Cs_2PbX_4–MSe_2 (X = Cl, Br, I; M = Mo, W) heterostructures using first-principles calculations. Firstly, six Cs_2PbX_4–MSe_2 interfaces remain stable in energy. With the halogen varying from Cl to I, the interlayer distances of Cs_2PbX_4–MSe_2 heterostructures increase rapidly. The CBM and VBM of monolayer Cs_2PbX_4 are all higher than that of monolayer MSe_2 and the charges transfer from Cs_2PbX_4 interfaces to MSe_2 interfaces when they contact. Both Cs_2PbX_4–MSe_2 heterostructures are type-II heterostructures, which can drive the photogenerated electrons and holes to move in opposite directions. What's more, Cs_2PbCl_4–$MoSe_2$ heterostructures exhibit the highest charge transport efficiency among Cs_2PbX_4–$MoSe_2$ heterostructures because Cs_2PbCl_4–$MoSe_2$ heterostructures have the lowest exciton binding energies among Cs_2PbX_4–MSe_2 heterostructures. In addition, the optical absorptions of all heterostructures are significantly higher than the corresponding Cs_2PbX_4 monolayers and MSe_2 monolayers. The construction of Cs_2PbX_4–$MoSe_2$ heterostructures is beneficial for improving the photoelectric performance of two-dimensional perovskite devices. Lastly, we found that the Cs_2PbI_4–WSe_2 heterostructure has the largest PCE (18%) among Cs_2PbX_4–MSe_2 heterostructures. The Cs_2PbCl_4–$MoSe_2$ heterostructure exhibits great potential application in photodetector devices and the Cs_2PbI_4–WSe_2 heterostructure has great potential application in solar cells.

Introduction

Solar energy is a renewable and clean energy source that can be used in the field of solar cells. In the early years, perovskites were considered to be one of the most promising solar cell materials.[1] Three-dimensional (3D) lead halide perovskites have been innovatively applied in the field of solar cells with power conversion efficiency (PCE) up to 25.6%.[2] The high PCE of 3D lead halide perovskites is because of their excellent photoelectric properties, such as high carrier mobility, large light absorption coefficient, long carrier diffusion length and strong photoluminescence.[3,4] Although the three-dimensional lead halide perovskites have great photoelectric properties, their instability in air limits their widespread use for commercialization.[5,6] In recent years, two-dimensional (2D) inorganic halide perovskites with good moisture resistance and stability have attracted attention for optoelectronic applications.[7] Currently, many theoretical studies and experiments on 2D perovskites have been conducted. For example, Ding *et al.* reported that the number of layers would affect the optical absorption and transport properties of 2D perovskite Cs_2PbI_4.[8] In addition, Bala *et al.* also revealed the same laws that the band gap and optical properties of 2D $Cs_{n+1}Pb_nX_{3n+1}$ (X = Cl, Br, I) perovskite vary with layer number.[9] In experiments, Song *et al.* fabricated 2D $CsPbBr_3$ nanosheets and used them to produce high-performance photodetectors.[10] These studies found that the bandgaps of 2D monolayer lead halide perovskites are larger than 3D lead halide perovskites, which lead to lower electric properties, optical absorption and low performance of optoelectronic applications.

Fortunately, two-dimensional monolayer lead halide perovskites have a wide range of photoelectric properties adjustable by replacing halogens, changing layers, and working with other two-dimensional materials. In particular, the halide perovskites grown in the other 2D materials provides excellent ability to further adjust band gaps, transport properties, charge carrier dynamics, chemical stability and optical light absorption.[11]

[a]State Key Laboratory of High Power Semiconductor Lasers, Changchun University of Science and Technology, Changchun 130013, China

[b]State Key Laboratory of Information Photonics and Optical Communications, Beijing University of Posts and Telecommunications, Beijing 100876, China

[c]School of Electronic Engineering, Beijing University of Posts and Telecommunications, Beijing 100876, China. E-mail: hanlhstar@bupt.edu.cn

[d]School of Information and Communication Engineering, Beijing University of Posts and Telecommunications, Beijing 100876, China. E-mail: guanxiaoning@bupt.edu.cn

Therefore, a great deal of scientific researches of 2D halide perovskites and 2D materials interface engineering have been carried to achieve low-cost, high efficiency, stable heterostructures photoelectric devices. For instance, He *et al.* theoretically studied the effects of different terminals of heterojunctions and found that $CsPbI_3/MoS_2$ heterostructure had higher electric performances than $CsPbI_3/WS_2$.[12] The WS_2–$CsPbBr_3$ heterostructure was applied to perovskite solar cells (PSCs), which significantly improved PSCs stability under constant light and humidity (80%) attack over.[13] While, the PCE of WS_2–$CsPbBr_3$ PSCs is only 10.65%.[13] Recently, inverted perovskite solar cells with WS_2 interlayers had increased PCE up to 21.1%.[14] As we can see, 2D lead halide perovskites applying for PSCs have high stability and can effectively improve PCE by coordinating with two-dimensional transition metal dichalcogenides (TMDs) such as WS_2, MoS_2 and so on.

$MoSe_2$ and WSe_2 as conventional materials of TMDs are widely used in interface engineering in experiments to improve optoelectronic properties of 2D organic halide perovskites. In experiments, Lu *et al.* fabricated a high-Performance WSe_2–$CH_3NH_3PbI_3$ perovskite photodetector.[15] $MoSe_2$–$CsPbBr_3$ Mixed van der Waals nanohybrids shown higher photocurrent than pure $CsPbBr_3$ nanocrystals.[16] Lee *et al.* found photoluminescence (PL) quenching occurred after the hybridization of perovskites with $MoSe_2$ and WSe_2 layers, which reflects the charge-transfer effect.[17] The PCE of PEDOT:PSS perovskite solar cells with WSe_2-mediated and without WSe_2-mediated is 16.3% and 13.8%, respectively.[18] These experiments observed the construction of TMDs and perovskite heterostructures can effectively improve the optoelectronic properties of halide perovskites. However, interface electronic transfer and band alignment of Cs_2PbX_4–MSe_2 heterostructures are not studied theoretically. It's worth revealing the effect of halide elements and MSe_2 (M = Mo, W) on Cs_2PbX_4–MSe_2 heterostructures, which can promote the development of 2D inorganic halide perovskite and TMDs optoelectronic applications.

Herein, we constructed the 2D inorganic halide perovskite Cs_2PbX_4 (X = Cl, Br, I) and monolayer MSe_2 heterostructures and discussed their stability, photoelectric properties and charge transfer mechanism through first-principles calculations. We studied electronic structures of the heterostructures with different halide elements and analysed the band alignment type for comparison. Next, we explore the charge transfers mechanism by calculating charge density difference. Finally, optical absorption coefficients of monolayer MSe_2, Cs_2PbX_4 and heterostructures Cs_2PbX_4–MSe_2 were calculated. Our results will be helpful to improve the application performance of two-dimensional lead halide perovskite and TMDs heterostructures.

Computational details

All the density functional theory calculations were performed with the Vienna Ab initial Simulation Package (VASP) code.[19,20] The projector-augmented wave (PAW) method was referred to electron–ion interactions.[21] The structure-relaxation, interface binding energy and optoelectronic properties were computed by Perdew, Burke and Ernzerhof's (PBE) exchange correlation function within the generalized gradient approximation (GGA) formalism.[22–26] The band gaps of monolayer perovskites and TMDs were further corrected using the screened Heyd–Scuseria–Ernzerhof (HSE) hybrid density functional with the spin–orbital coupling (SOC). The plane wave basis set with a cutoff energy of 450 eV. The convergence criteria were 1×10^{-4} eV for the self-consistent field energy and 0.01 eV Å^{-1} for the residual forces on each atom, respectively. A vacuum of 20 Å was considered along *z* direction to avoid artificial interlayer interactions. 3 × 6 × 1 *k*-sampling generated by the Monkhorst–Pack scheme for the Brillouin zone was adopted. The zero damping DFT-D3 method of Gimme is used to account for correcting the van der Waals interaction of Heterostructure.

The interface binding energy is calculated by the following formula:

$$E_b = (E_{heter.} - E_{Cs_2PbX_4} - E_{MSe_2})/A \quad (1)$$

where *A* represents the interfacial area of Cs_2PbX_4–MSe_2 heterostructures, $E_{heter.}$, $E_{Cs_2PbX_4}$, E_{MSe_2} are the total energy of heterostructures Cs_2PbX_4–MSe_2, monolayer Cs_2PbX_4 and MSe_2, respectively.

The plane-averaged charge density difference $\Delta\rho$ is calculated as the followed equation:

$$\Delta\rho(z) = \rho_{heter.} - \rho_{Cs_2PbX_4} - \rho_{MSe_2} \quad (2)$$

where $\rho_{heter.}$, $\rho_{Cs_2PbX_4}$ and ρ_{MSe_2} correspond to the plane-averaged charge density of heterojunctions Cs_2PbX_4–MSe_2, monolayer Cs_2PbX_4 and MSe_2, respectively.

The 2D Mott–Wananier (MW) exciton binding energy (E_{eb}) equation is calculated as the followed equation:

$$E_{eb} = 4\frac{13.6\mu_{ex}}{m_0\varepsilon^2}\text{eV} \quad (3)$$

where μ_{ex} is the effective exciton mass ($\mu_{ex} = m_e m_h/(m_e + m_h)$), m_0 is the electron mass, and ε is the static dielectric constant. The effective masses of electron (m_e) and hole (m_h) are determined by the curvature of the energy band extremum.

The optical absorption coefficients are obtained from dielectric function, as the followed equation represented:

$$\alpha(\omega) = \left(\sqrt{2}\right)\omega\left[\sqrt{\varepsilon_1(\omega)^2 + \varepsilon_2(\omega)^2} - \varepsilon_1(\omega)^2\right]^{1/2} \quad (4)$$

$$\varepsilon(\omega) = \varepsilon_1(\omega) + i\varepsilon_2(\omega) \quad (5)$$

where α, ω correspond to the optical absorption coefficient, the angular frequency and the dielectric function $\varepsilon(\omega)$ contains real part $\varepsilon_1(\omega)$ and imaginary part $\varepsilon_2(\omega)$.

Results and discussion

In recent years, the 2D inorganic perovskites Cs_2PbX_4 (X = Cl, Br, I) and monolayers MSe_2 (M = Mo, W) have been successfully synthesized, which attracted much attention due to its highly stable structures.[7,27,28] The unit cell of Cs_2PbX_4 perovskites belongs to cubic system and the optimized lattice parameters of monolayer Cs_2PbCl_4, Cs_2PbBr_4, Cs_2PbI_4 is 5.64 Å, 5.91 Å and 6.30 Å, respectively.[29] $[CsI]^0$ interface exhibits more strongly charge transferring than $[PbI_2]^0$.[30] Therefore the $[CsI]^0$ plane of the monolayer Cs_2PbX_4 is used to form the heterojunctions. The optimized lattice parameters of monolayer $MoSe_2$, WSe_2 are 3.32 Å.[31–33] To minimize the lattice mismatch between the stacking blocks, the supercell of new Cs_2PbX_4–MSe_2 heterostructures are built by 3×1 cubic phases Cs_2PbCl_4 and $5 \times \sqrt{3}$ MSe_2, $\sqrt{8} \times 2$ cubic phases Cs_2PbBr_4 and $5 \times \sqrt{13}$ MSe_2, and $\sqrt{8} \times \sqrt{2}$ cubic phases Cs_2PbI_4 and $\sqrt{31} \times \sqrt{7}$ MSe_2, respectively, as seen in Fig. 1 (Table 1).

The lattice mismatches of Cs_2PbCl_4–$MoSe_2$, Cs_2PbBr_4–$MoSe_2$, Cs_2PbI_4–$MoSe_2$, Cs_2PbCl_4–WSe_2, Cs_2PbBr_4–WSe_2 and Cs_2PbI_4–WSe_2 heterostructures are less than 1.10%, 0.62%, 1.79%, 1.02%, 0.65% and 1.82%. The optimized vertical interlayer distances of Cs_2PbCl_4–$MoSe_2$, Cs_2PbBr_4–$MoSe_2$, Cs_2PbI_4–$MoSe_2$, Cs_2PbCl_4–WSe_2, Cs_2PbBr_4–WSe_2 and Cs_2PbI_4–WSe_2 interfaces are 3.07, 3.12, 3.16, 2.90, 3.18 and 3.30 Å, respectively, which increase gradually with the halogen varying from Cl to I. Interface binding energy of Cs_2PbCl_4–$MoSe_2$, Cs_2PbBr_4–$MoSe_2$ and Cs_2PbI_4–$MoSe_2$, Cs_2PbCl_4–WSe_2, Cs_2PbBr_4–WSe_2 and Cs_2PbI_4–WSe_2 interfaces is −16.73, −16.28 and −16.12, −17.09, −17.52 and −15.56 meV Å^{-2}, respectively. The small interface binding energy and the interlayer distance ranging from 2.9 Å to 3.3 Å indicate that 2D Cs_2PbX_4–MSe_2 heterostructures are formed by vdW contact.[33] These E_b values are comparable to E_b of InSe/GaSe (−18.25 meV Å^{-2}), suggesting that Cs_2PbX_4–MSe_2 heterostructures are stable in energy.[34] In addition, $MoSe_2$–$CsPbBr_3$ Mixed van der Waals nanohybrids also have been fabricated in experiments (Table 2).[16]

In order to study the band structures of Cs_2PbX_4–MSe_2 heterostructures, the band structures of 2D perovskites Cs_2PbX_4, monolayer WSe_2 and monolayer $MoSe_2$ were calculated by different functionals, including PBE, PBE with SOC (PBE + SOC), HSE, and HSE with SOC (HSE + SOC) functionals. Monolayer $MoSe_2$ and monolayer WSe_2 show a direct band gap of 1.45 eV and 1.56 eV using PBE functional. Monolayer Cs_2PbCl_4, Cs_2PbBr_4 and Cs_2PbI_4 possess a direct bandgap of 2.59 eV, 2.18 eV and 1.84 eV using PBE functional. We find that the bandgaps of Cs_2PbX_4 computed *via* PBE and HSE + SOC functionals are in good agreements with experiments and other theoretical results.[9,10,27,28,35–38] The band gap calculated by HSE is larger than PBE and the band gap calculated by PBE + SOC is smaller than PBE. In addition, the band gap of MSe_2 calculated by HSE + SOC is larger than the related experimental data.[27,28] This is because the HSE functional usually overcorrects slightly the band gap of an intrinsic semiconductor.[39] Thus, in order to accurately and closely study the contact characteristics of Cs_2PbX_4–MSe_2 heterostructures, PBE is employed in the following heterostructures section. When monolayers Cs_2PbX_4 and MSe_2 (M = Mo, W) are contacted to make up Cs_2PbX_4–MSe_2 heterostructures, the electronic structures of Cs_2PbX_4–MSe_2 heterostructures are shown in Fig. 2. The Cs_2PbCl_4–$MoSe_2$, Cs_2PbBr_4–$MoSe_2$, Cs_2PbI_4–$MoSe_2$, Cs_2PbCl_4–WSe_2, Cs_2PbBr_4–WSe_2 and Cs_2PbI_4–WSe_2 heterostructures have an indirect bandgap with the value of 1.30 eV, 1.48 eV, 1.54 eV, 1.33 eV, 1.67 eV and 1.53 eV, which approach optimal bandgap (1.34 eV) for solar cells.[40] Moreover, the conduction band minimum (CBM) of Cs_2PbX_4–MSe_2 heterostructures are dominated by the MSe_2 layer and the valence band maximum (VBM) of Cs_2PbX_4–MSe_2 heterostructures are dominated by Cs_2PbX_4 part.

The analysis of energy level arrangement is of great significance to further study interface properties of Cs_2PbX_4–MSe_2 heterostructures. The vacuum energy level (E_v) is set to zero in the precontact state and the Fermi level (E_f) is set to zero in the contact state. In precontact state, the CBM and VBM of monolayer Cs_2PbX_4 are both higher than that of monolayer MSe_2 and both Cs_2PbX_4–MSe_2 are type-II heterostructures, as seen in Fig. 3(a). The electrons will diffuse from monolayers Cs_2PbX_4 to monolayers MSe_2 and the holes will move from monolayers MSe_2 monolayer to monolayers s_2PbX_4 when they contact. Correspondingly, the holes accumulate in Cs_2PbX_4 monolayers and the electrons accumulate in MSe_2 monolayers. Moreover, the difference between the vacuum level and the Fermi level is defined as the work function.[31] The work function is the internal dynamics of electron flow. The computed work functions of monolayers Cs_2PbCl_4, Cs_2PbBr_4, Cs_2PbI_4, $MoSe_2$ and WSe_2 are 4.08 eV, 4.21 eV, 4.30 eV, 4.83 eV and 4.51 eV, respectively. The heterostructures are mainly related to the work function after contact. In order to maintain Fermi levels at the same level after contact, the Fermi level of all Cs_2PbX_4 perovskites moved down and the Fermi level of monolayer MSe_2 moved up after they contact each other.

The energy level diagram of Cs_2PbX_4–MSe_2 heterostructures in contact states is given in Fig. 3(b). The Cs_2PbX_4–MSe_2 heterostructures are type-II heterostructures, which can drive the photogenerated holes and electrons to move in opposite directions, resulting in spatial separation of holes and electrons on different sides of heterostructures.[33] Thus, Cs_2PbX_4–MSe_2 heterostructures are beneficial for improving the photoelectric conversion efficiency of Cs_2PbX_4–MSe_2 optoelectronic applications. In these type-II heterostructures, the differences between the VBM of their components (valence band offset, $\Delta\nu$) are crucial for hole blocking and the differences between the CBM

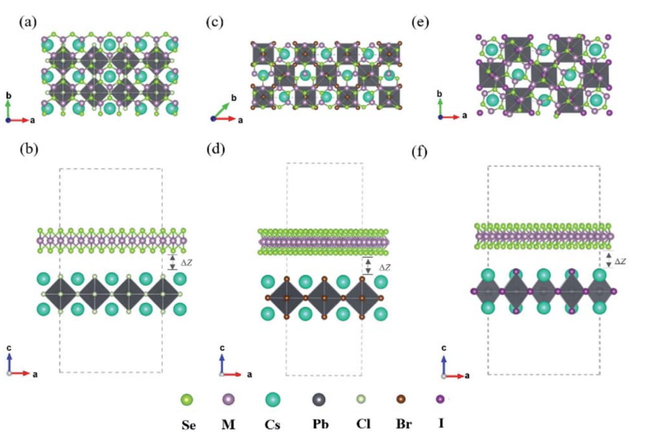

Fig. 1 Top and side views of relaxed Cs_2PbX_4–MSe_2 (M = Mo, W) heterostructures. (a and b) Cs_2PbCl_4–MSe_2 heterostructure. (c and d) Cs_2PbBr_4–MSe_2 heterostructure. (e and f) Cs_2PbI_4–MSe_2 heterostructure.

Table 1 Optimized lattice parameters (a and b) and expanded cell lattice parameters (a_1 and b_1), lattice mismatch, interlayer distance ΔZ and interface binding energy E_b of the relaxed Cs_2PbX_4–WSe_2 heterostructures

Heterostructures	a (Å)	b (Å)	a_1 (Å)	b_1 (Å)	Mismatch (%)	ΔZ (Å)	E_b (meV Å^{-2})
Cs_2PbCl_4–$MoSe_2$	16.51	5.66	16.75	5.69	1.10%	3.09	−16.73
Cs_2PbBr_4–$MoSe_2$	16.35	11.81	16.65	11.89	0.62%	3.12	−16.28
Cs_2PbBr_4–$MoSe_2$	18.22	8.66	18.14	8.84	1.79%	3.16	−16.12
Cs_2PbBr_4–WSe_2	16.41	5.67	16.75	5.69	1.02%	2.90	−17.09
Cs_2PbBr_4–WSe_2	16.35	11.81	16.65	11.89	0.65%	3.18	−17.52
Cs_2PbBr_4–WSe_2	18.21	8.66	18.20	8.67	1.82%	3.30	−15.56

Table 2 The bandgaps of monolayer Cs_2PbX_4, $MoSe_2$ and WSe_2 by different calculation method

Functional	Cs_2PbCl_4	Cs_2PbBr_4	Cs_2PbI_4	$MoSe_2$	WSe_2
PBE	2.59	2.18	1.84	1.45	1.56
HSE	3.58	2.91	2.57	2.10	2.03
PBE + SOC	1.84	1.46	1.09	1.37	1.33
HSE + SOC	2.78	2.14	1.78	1.89	1.93
Experiment	3.01	2.32	1.86	1.48	1.60

of their components (conduction band offset, Δc) are crucial for electron transport. The large $\Delta \nu$ promotes hole extraction from TMDs layers to perovskite layers and the large Δc allows free electrons to move from perovskite to TMDs layers. It is shown that Cs_2PbCl_4–MSe_2 heterostructure have the largest Δc and $\Delta \nu$ among Cs_2PbX_4–MSe_2 heterostructures.[12] Thus, the Cs_2PbCl_4–$MoSe_2$, and Cs_2PbCl_4–WSe_2 heterostructures may have the largest charge transport power and are more conducive to reducing the dark current. In addition, Cs_2PbX_4–$MoSe_2$ heterostructures have lager Δc and $\Delta \nu$ than Cs_2PbX_4–WSe_2 heterostructures.

In addition, the Mott–Wananier theory has been used to approximate exciton binding energies in the vdW heterostructures.[41] Table 3 lists the carrier masses and MW exciton binding energy of Cs_2PbX_4–MSe_2 heterostructures. The lower exciton binding energies usually facilitate the splitting of excitons into free charge carriers.[34] It is shown that Cs_2PbCl_4–$MoSe_2$ heterostructures exhibit the lowest exciton binding energies among Cs_2PbX_4–$MoSe_2$ heterostructures. Therefore, Cs_2PbCl_4–$MoSe_2$ heterostructures can effectively promotes the separation of excitons and exhibit the highest charge transport efficiency among Cs_2PbX_4–MSe_2 heterostructures.

To clearly investigate the recombination rates of electron–hole pairs and transfer of charges between the Cs_2PbX_4 monolayers and MSe_2 monolayers across the interfaces, the plane-averaged charge density difference $\Delta \rho$ are calculated, as shown in Fig. 4. The results demonstrate that the holes mainly accumulated at the Cs_2PbX_4 interfaces and the charges accumulated at MSe_2 interfaces. Additionally, the charges transfer

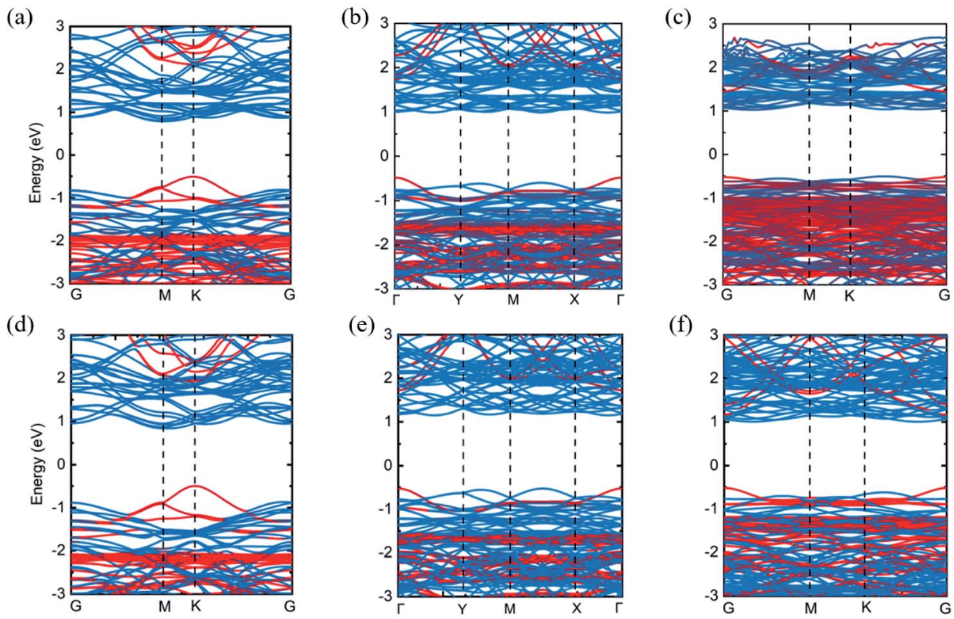

Fig. 2 Band structures of Cs_2PbX_4–MSe_2 heterostructures (a) X = Cl, M = Mo; (b) X = Br, M = Mo; (c) X = I, M = Mo; (d) X = Cl, M = W; (e) X = Br, M = W; (f) X = I, M = W. The red and blue lines correspond to Cs_2PbX_4 and MSe_2, respectively.

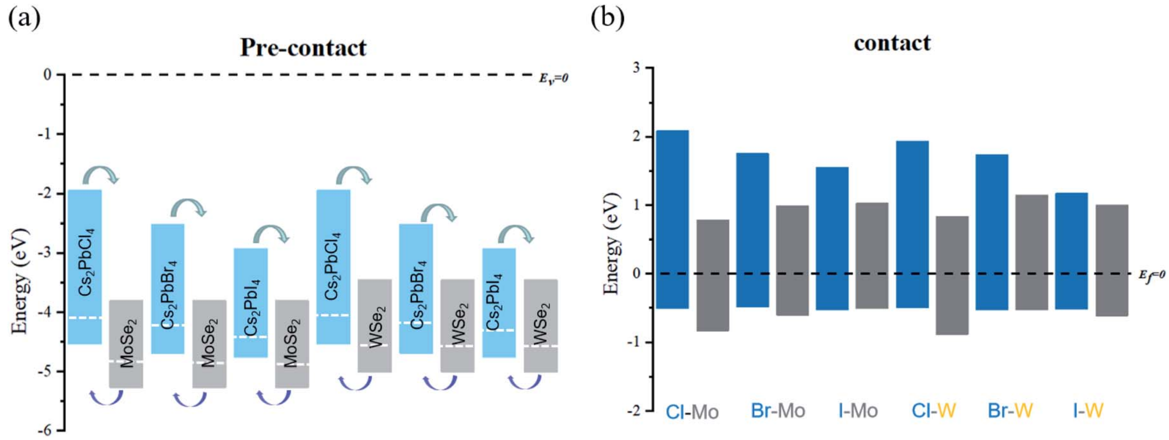

Fig. 3 Energy level graphs of the monolayer MSe_2 and Cs_2PbX_4 in the precontact (a) and contact (b). Blue and gray rectangles represent the monolayer Cs_2PbX_4 and MSe_2. The bottom and top of rectangles correspond to VBM and CBM, respectively.

Table 3 Carrier effective masses (m_e, m_h, and μ_{ex}), static dielectric constant (ε) and MW excitonic binding energies (E_{eb})

Heterostructures	m_e (m_0)	m_h (m_0)	μ_{ex} (m_0)	ε	E_{eb} (eV)
Cs_2PbCl_4–$MoSe_2$	1.16	0.28	0.23	5.34	0.43
Cs_2PbBr_4–$MoSe_2$	0.79	0.71	0.37	5.44	0.68
Cs_2PbI_4–$MoSe_2$	1.39	0.67	0.45	5.24	1.00
Cs_2PbCl_4–WSe_2	1.46	0.27	0.23	4.95	0.50
Cs_2PbBr_4–WSe_2	0.75	0.66	0.35	5.08	0.74
Cs_2PbI_4–WSe_2	1.03	0.61	0.38	5.26	0.76

from Cs_2PbX_4 interfaces to MSe_2 interfaces while the holes move in the opposite direction. The direction of charge transfer is consistent with that of band alignment analysis, which shown type-II heterostructures are benefited to the separation of electrons and holes. What's more, detail charge transfers among interlayer spacing are used to quantitatively evaluate charge transferring of heterostructures. The Cs_2PbCl_4–$MoSe_2$, Cs_2PbBr_4–$MoSe_2$, Cs_2PbI_4–$MoSe_2$, Cs_2PbCl_4–WSe_2, Cs_2PbBr_4–WSe_2 and Cs_2PbI_4–WSe_2 heterostructures have charge transfers among interlayer spacing with the values of 0.18, 0.15, 0.16, 0.16, 0.10 and 0.14 $\times$ $10^{-3}e$. We find that the Cs_2PbCl_4–MSe_2 heterostructures have the highest charge transfers in the six Cs_2PbX_4–MSe_2 heterostructures among interlayer spacing. In addition, Cs_2PbX_4–$MoSe_2$ heterostructures have larger charge transfers than Cs_2PbX_4–WSe_2 heterostructures. It is because

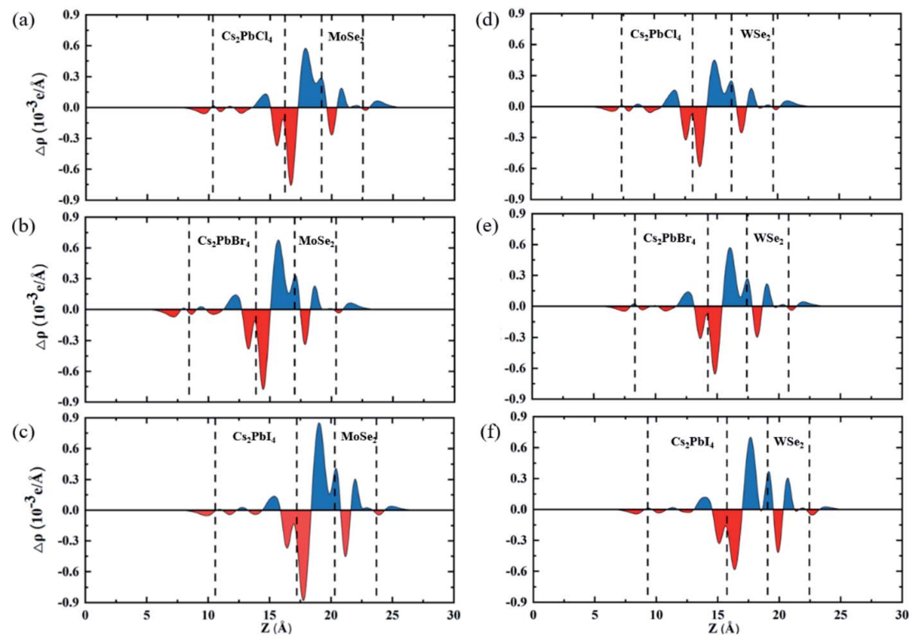

Fig. 4 The planar-averaged differential charge density $\Delta\rho(z)$ of Cs_2PbX_4–MSe_2 heterostructures: (a and d) X = Cl; (b and e) X = Br; (c and f) X = I. Red and blue represent electron depletion and accumulation.

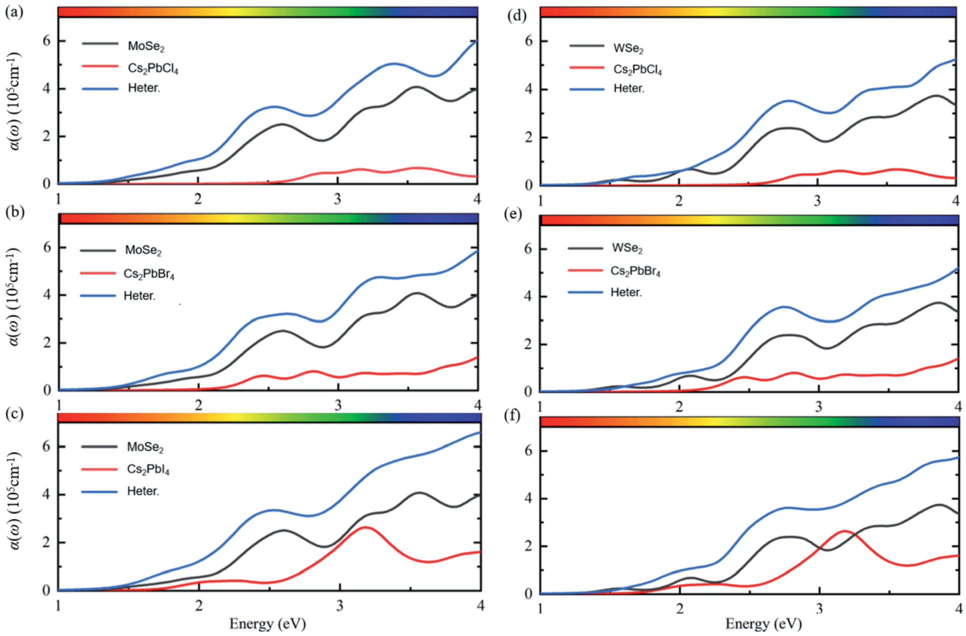

Fig. 5 Optical absorption coefficients of (a and d) Cs_2PbCl_4–MSe_2, (b and e) Cs_2PbBr_4–MSe_2, and (c and f) Cs_2PbI_4–MSe_2 heterostructures. The blue, black and red lines represent optical absorption spectrum of heterostructures, monolayer MSe_2 and Cs_2PbX_4, respectively.

Cs_2PbX_4–$MoSe_2$ heterostructures have smaller exciton binding energies than Cs_2PbX_4–WSe_2 heterostructures.

Except for the electronic structures and charge redistributions of heterostructures, the optical properties in vdW heterostructures have important effects on the performance of perovskite optoelectronic devices.[42] In order to further study the optical properties of Cs_2PbX_4–MSe_2 heterostructures, the optical absorption coefficients were calculated, as shown in Fig. 5. The optical absorption coefficients of MSe_2 monolayers are higher than those of Cs_2PbX_4 monolayers. The optical absorption coefficients of all heterostructures are significantly higher than those of corresponding Cs_2PbX_4 monolayers and MSe_2 monolayers. This is because the bandgaps of 2D Cs_2PbX_4–MSe_2 heterostructures are smaller than the bandgaps of Cs_2PbX_4 monolayers. The bandgaps of Cs_2PbX_4–MSe_2 heterostructures approach optimal bandgap (1.34 eV) for solar cells.[40] Thus, the construction of Cs_2PbX_4–MSe_2 heterostructures is beneficial to improve the light absorption of optoelectronic devices.

In addition, the light absorption of Cs_2PbX_4–$MoSe_2$ heterostructures is only slightly greater than that of Cs_2PbX_4–WSe_2 in the visible region because the light absorption of $MoSe_2$ is slightly greater than that of WSe_2 in the visible region. The light absorption coefficients of Cs_2PbX_4 increase rapidly in the visible

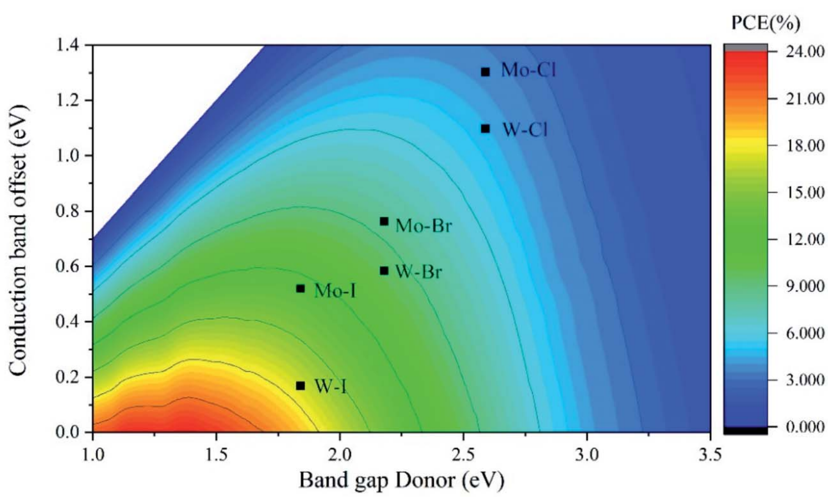

Fig. 6 Contour plot showing the calculated PCE of Cs_2PbX_4–MSe_2 heterostructures according to the Cs_2PbX_4 donor band gap and conduction band offset Δ*c*.

region with the halogen varying from Cl to I. The light absorption coefficients of $Cs_2PbX4–MSe_2$ heterostructures increase rapidly in the visible region with the halogen varying from Cl to I. Therefore, the $Cs_2PbI_4–MSe_2$ heterostructure has great potential application in solar cells among $Cs_2PbX_4–MSe_2$ heterostructures.

In order to explore the application of $Cs_2PbX_4–MSe_2$ heterostructures in solar cells, we further calculated the power conversion efficiency of $Cs_2PbX_4–MSe_2$ heterostructures. The PCE depends on the donor band gap and conduction band offset.[43,44] The PCE of $Cs_2PbX_4–MSe_2$ heterostructures with type-II alignment is shown in Fig. 6 as a contour plot where the *x*- and *y*-axes are the donor band gap and conduction band offset, respectively. The PCE of $Cs_2PbI_4–MoSe_2$, $Cs_2PbI_4–WSe_2$ and $Cs_2PbBr_4–WSe_2$ heterostructures is 13%, 18% and 10%, which is greater than 10%. Three heterostructures can be used in solar cells. $Cs_2PbI_4–WSe_2$ heterostructure has the largest PCE (18%) among $Cs_2PbX_4–MSe_2$ heterostructures. The PCE of $Cs_2PbI_4–WSe_2$ heterostructure is larger than that of $WS_2/CsPbBr_3$ PSCs (10.65%) and WSe_2–mediated PSCs (16.3%).[13,18] With the halogen varying from Cl to I, the PCE of $Cs_2PbX_4–WSe_2$ heterostructures increase rapidly. The PCE variation trend is consistent with the absorption coefficients of $Cs_2PbX_4–MSe_2$ heterostructures varying from Cl to I. In addition, the PCE of $Cs_2PbX_4–WSe_2$ heterostructures is larger than the PCE of $Cs_2PbX_4–MoSe_2$ heterostructures. This is mainly because $Cs_2PbX_4–WSe_2$ heterostructures have smaller Δc than $Cs_2PbX_4–MoSe_2$ heterostructures. Therefore, $Cs_2PbI_4–WSe_2$ heterostructure has great potential application in solar cells.

Conclusions

In summary, we have systematically studied the structural, stability, charge transfer and optoelectronic properties of 2D perovskite $Cs_2PbX_4–MSe_2$ heterostructures with different halide elements based on density functional calculations. All these six heterostructures are stable in energy and the interlayer distances increase gradually with the halogen varying from Cl to I. Electronic structures show $Cs_2PbX_4–MSe_2$ heterostructures belongs to type-II energy level shifts with narrower optical gap than monolayers Cs_2PbX_4. In addition, the $Cs_2PbCl_4–MoSe_2$, and $Cs_2PbCl_4–WSe_2$ heterostructures may have the largest charge transport power due to their larger band offset, which is beneficial to reduce dark current and improve open circuit voltage. $Cs_2PbCl_4–MoSe_2$ heterostructures can effectively promotes the separation of excitons and exhibit the highest charge transport efficiency among $Cs_2PbX_4–MSe_2$ heterostructures due to their lowest exciton binding energies. $Cs_2PbCl_4–MoSe_2$ heterostructure has the potential to be applied in photodetectors. Next, the charges transfer from Cs_2PbX_4 interfaces to MSe_2 interfaces while the holes move in the opposite direction. The holes mainly accumulated at the Cs_2PbX_4 interfaces and the charges accumulated at MSe_2 interfaces. $Cs_2PbX_4–MoSe_2$ heterostructures have larger charge transfers than $Cs_2PbX_4–WSe_2$ heterostructures. Finally, optical absorptions of six heterostructures are significantly higher than the corresponding Cs_2PbX_4 monolayers and MSe_2 monolayers. The PCE of $Cs_2PbX_4–WSe_2$ heterostructures is larger than the PCE of $Cs_2PbX_4–MoSe_2$ heterostructures. $Cs_2PbI_4–WSe_2$ heterostructure has the largest PCE (18%) among $Cs_2PbX_4–MSe_2$ heterostructures. In conclusion, $Cs_2PbCl_4–MoSe_2$ heterostructure exhibits great potential application in photodetectors devices and $Cs_2PbI_4–WSe_2$ heterostructure has great potential application in solar cells. Our findings provide insight into of $Cs_2PbX_4–MSe_2$ heterostructures can effectively improve the performance of perovskite optoelectronic devices.

Conflicts of interest

There are no conflicts to declare.

Acknowledgements

This work is supported by the Fund of State Key Laboratory of IPOC(BUPT) (no. IPOC2019ZZ04) and the Open-Foundation of Key Laboratory of Laser Device Technology, China North Industries Group Corporation Limited (Grant No. KLLDT202103). We thank for the helpful discussion with Prof. Pengfei Guan and the computational support from the Beijing Computational Science Research Center (CSRC). We also acknowledge the computation supported by High-performance Computing Platform of BUPT.

Notes and references

1 A. T. Barrows, A. J. Pearson, C. K. Kwak, A. D. F. Dunbar, A. R. Buckley and D. G. Lidzey, *Energy Environ. Sci.*, 2014, **7**, 2944–2950.
2 K. Xiao, R. Lin, Q. Han, Y. Hou, Z. Qin, H. T. Nguyen, J. Wen, M. Wei, V. Yeddu, M. I. Saidaminov, Y. Gao, X. Luo, Y. Wang, H. Gao, C. Zhang, J. Xu, J. Zhu, E. H. Sargent and H. Tan, *Nat. Energy*, 2020, **5**, 870–880.
3 I. L. Braly, D. W. deQuilettes, L. M. Pazos-Outon, S. Burke, M. E. Ziffer, D. S. Ginger and H. W. Hillhouse, *Nat. Photonics*, 2018, **12**, 355–361.
4 M. M. Lee, J. Teuscher, T. Miyasaka, T. N. Murakami and H. J. Snaith, *Science*, 2012, **338**, 643–647.
5 J. H. Noh, S. H. Im, J. H. Heo, T. N. Mandal and S. I. Seok, *Nano Lett.*, 2013, **13**, 1764–1769.
6 Y.-Y. Zhang, S. Chen, P. Xu, H. Xiang, X.-G. Gong, A. Walsh and S.-H. Wei, *Chin. Phys. Lett.*, 2018, **35**, 036104.
7 S. Chen and G. Shi, *Adv. Mater.*, 2017, **29**, 1605448.
8 Y. F. Ding, Q. Q. Zhao, Z. L. Yu, Y. Q. Zhao, B. Liu, P. B. He, H. Zhou, K. L. Li, S. F. Yin and M. Q. Cai, *J. Mater. Chem. C*, 2019, **7**, 7433–7441.
9 A. Bala, A. K. Deb and V. Kumar, *J. Phys. Chem. C*, 2018, **122**, 7464–7473.
10 J. Song, L. Xu, J. Li, J. Xue, Y. Dong, X. Li and H. Zeng, *Adv. Mater.*, 2016, **28**, 4861–4869.
11 E. Shi, Y. Gao, B. P. Finkenauer, A. Akriti, A. H. Coffey and L. Dou, *Chem. Soc. Rev.*, 2018, **47**, 6046–6072.
12 J. He, J. Su, Z. Lin, S. Zhang, Y. Qin, J. Zhang, J. Chang and Y. Hao, *J. Phys. Chem. C*, 2019, **123**, 7158–7165.

13 Q. W. Zhou, J. L. Duan, X. Y. Yang, Y. Y. Duan and Q. W. Tang, *Angew. Chem., Int. Ed.*, 2020, **132**, 22181–22185.
14 J. P. Cao, G. Q. Tang, P. You, T. Y. Wang, F. Y. Zheng, J. Zhao and F. Yan, *Adv. Funct. Mater.*, 2020, **30**, 2002358.
15 Hybrid Bilayer WSe_2-$CH_3NH_3PbI_3$ Organolead Halide Perovskite as a High-Performance Photodetector.
16 S. Hassan, P. Basera, S. Bera, M. Mittal, S. K. Ray, S. Bhattacharya and S. Sapra, *ACS Appl. Mater. Interfaces*, 2020, **12**, 7217–7325.
17 S.-H. Lee, J. Y. Kim, S. Choi, Y. Lee, K.-S. Lee, J. Kim and J. Joo, *ACS Appl. Mater. Interfaces*, 2020, **12**, 25159–25167.
18 Y. Choi, S. Jung, N. K. Oh, J. Lee, J. Seo, U. Kim, D. Koo and H. Park, Enhanced charge transport via metallic 1T phase transition metal dichalcogenides-mediated hole transport layer engineering for perovskite solar cells, *Chemnanomat*, 2019, **5**, 1050–1058.
19 G. Kresse and D. Joubert, *Phys. Rev. B: Condens. Matter Mater. Phys.*, 1999, **59**, 1758–1775.
20 J. P. Perdew, K. Burke and M. Ernzerhof, *Phys. Rev. Lett.*, 1996, **77**, 3865–3868.
21 P. E. Blochl, *Phys. Rev. B: Condens. Matter Mater. Phys.*, 1994, **50**, 17953–17979.
22 B. Jia, P. Zhu, S. Sun, L. Han, G. Liu, Y. Wang, G.-D. Peng and P. Lu, *IEEE J. Sel. Top. Quantum Electron.*, 2019, **26**, 1–6.
23 S. Lin, J. C. Liu, W. Z. Li, D. Wang, Y. Huang, C. Jia, Z. W. Li, H. Y. Wang, J. N. Song, Z. L. Liu, K. Huang, D. Zu, M. Lei, B. Hong and H. Wu, *Nano Lett.*, 2019, **19**, 6853–6861.
24 J. C. Xu, K. Bi, R. Zhang, Y. N. Hao, C. W. Lan, M.-M. Klaus, X. J. Zhai, Z. D. Zhang and S. G. H, *Research*, 2019, **2019**, 9686213.
25 X. N. Guan, R. Zhang, B. N. Jia, L. Y. Wu, B. Zhou, L. Fan, G. Liu, Y. Wang, P. F. Lu and G. D. Peng, *J. Non-Cryst. Solids*, 2020, **550**, 120388.
26 P. F. Lu, *J. Sichuan Norm. Univ., Nat. Sci.*, 2020, **43**, 1–20.
27 X. Wang, Y. Gong, G. Shi, W. L. Chow, K. Keyshar, G. Ye, R. Vajtai, J. Lou, Z. Liu, E. Ringe, B. K. Tay and P. M. Ajayan, *ACS Nano*, 2014, **8**, 5125–5131.
28 J.-K. Huang, J. Pu, C.-L. Hsu, M.-H. Chiu, Z.-Y. Juang, Y.-H. Chang, W.-H. Chang, Y. Iwasa, T. Takenobu and L.-J. Li, *ACS Nano*, 2014, **8**(1), 923–930.
29 J.-H. Yang, Q. Yuan and B. I. Yakobson, *J. Phys. Chem. C*, 2016, **120**, 24682–24687.
30 Y.-Q. Zhao, Y. Xu, D.-F. Zou, J.-N. Wang, G.-F. Xie, B. Liu, M.-Q. Cai and S.-L. Jiang, *J. Phys.: Condens. Matter*, 2020, **32**, 195501.
31 Y. Ding, Y. Wang, J. Ni, L. Shi, S. Shi and W. Tang, *Phys. Chem. Chem. Phys.*, 2011, **13**, 15546–15553.
32 Y. Zhang, Y. Zhao, Y. Xu and L. He, *Solid State Commun.*, 2021, **327**, 114233.
33 B. Liu, M. Long, M.-Q. Cai and J. Yang, *J. Phys. Chem. Lett.*, 2018, **327**, 114233.
34 J. H. Chen, X. J. He, B. S. Sa, J. Zhou, C. Xu, C. L. Wen and Z. M. Sun, *Nanoscale*, 2019, **11**, 6431–6444.
35 P. Zhu, H. Zhao, X. Li, Y. Zu, L. Wu, C. Chen and G. Liu, *Phys. E*, 2021, **134**, 114908.
36 A. Molina-Sanchez, *ACS Appl. Energy Mater.*, 2018, **1**, 6361–6367.
37 Z. Zheng, X. X. Wang, Y. W. Shen, Z. Y. Luo, L. G. Li, L. Gan, Y. Ma, H. Q. Li, A. L. Pan and T. Y. Zhai, *Adv. Opt. Mater.*, 2018, **6**, 1800879.
38 P. B. Gui, H. Zhou, F. Yao, Z. H. Song, B. R. Li and G. J. Fang, *Small*, 2019, **15**, 1902618.
39 R. J. Sutton, M. R. Filip, A. A. Haghighirad, N. Sakai, B. Wenger, F. Giustino and H. J. Snaith, *ACS Energy Lett.*, 2018, **3**, 1787–1794.
40 S. Ruhle, *Sol. Energy*, 2016, **130**, 139–147.
41 P. Wang, Y. X. Zong, H. Liu, H. Y. Wen, H. X. Deng, Z. M. Wei, H. B. Wu and J. B. Xia, *J. Phys. Chem. C*, 2020, **214**, 23832–23838.
42 W. J. Yin, J. H. Yang, J. Kang, Y. Yan and S. H. Wei, *J. Mater. Chem. A*, 2015, **3**, 8926–8942.
43 M. C. Scharber, D. Wuhlbacher, M. Koppe, P. Denk, C. Waldauf, A. J. Heeger and C. L. Brabec, *Adv. Mater.*, 2006, **18**, 189.
44 M. Bernardi, M. Palummo and J. C. Grossman, *ACS Nano*, 2012, **6**, 10082–10089.